

Article

# Analysis of Peak Ground Acceleration and Seismogenic Fault Characteristics of the Mw7.8 Earthquake in Turkey

Yushi Duan <sup>1,2,\*</sup> , Jingshan Bo <sup>1,2</sup>, Da Peng <sup>1</sup>, Qi Li <sup>1</sup>, Wei Wan <sup>1,2</sup> and Wenhao Qi <sup>1</sup>

<sup>1</sup> Key Laboratory of Earthquake Engineering and Engineering Vibration, Institute of Engineering Mechanics, China Earthquake Administration, Harbin 150080, China; pengda1992@gmail.com (D.P.); liqilq96@163.com (Q.L.); wanshiruyi516@126.com (W.W.)

<sup>2</sup> Institute of Disaster Prevention, Sanhe 065201, China

\* Correspondence: duanyushi2023@163.com

**Featured Application:** This paper investigates the peak ground acceleration (PGA) and seismogenic fault characteristics of the Mw7.8 earthquake that struck Turkey on 6 February 2023. The paper identifies the near-fault effect, the fault locking segment effect, and the trampoline effect of the earthquake, and presents a detailed spatial distribution of PGA. The featured application of this work is in seismic engineering and disaster prevention, where the PGA and fault characteristics are essential for assessing the seismic demand and capacity of structures, as well as the potential damage and loss induced by earthquakes. This paper also enhances the understanding of the seismogenic mechanism, damage mode, characteristics, and strong earthquake law of the Turkey earthquake, which can facilitate the improvement of the seismic design codes and emergency response plans in Turkey and other regions with similar tectonic settings.

**Abstract:** A Mw7.8 earthquake struck Turkey on 6 February 2023, causing severe casualties and economic losses. This paper investigates the characteristics of strong ground motion and seismogenic fault of the earthquake. We collected and processed the strong ground motion records of 379 stations using Matlab, SeismoSignal, and Surfer software: Matlab (Version R2016a), SeismoSignal (Version 5.1.0), and Surfer (Version 23.0.15), and obtained the peak ground acceleration (PGA) contour map. We analyzed the near-fault effect, the fault locking segment effect, and the trampoline effect of the earthquake based on the spatial distribution of PGA, the fault geometry, and slip distribution. We found that the earthquake generated a very strong ground motion concentration effect in the near-fault area, with the maximum PGA exceeding 2000 cm/s<sup>2</sup>. However, the presence of fault locking segments influenced the spatial distribution of ground motion, resulting in four significant PGA high-value concentration areas at a local dislocation, a turning point, and the end of the East Anatolian Fault. We also revealed for the first time the typical manifestation of the trampoline effect in this earthquake, which was characterized by a large vertical acceleration with a positive direction significantly larger than the negative direction. This paper provides an important reference for understanding the seismogenic mechanism, damage mode, characteristics, and strong earthquake law of the Turkey earthquake.

**Keywords:** Turkey earthquake; peak ground acceleration; seismogenic fault; near-fault effect; fault locking segment effect; trampoline effect

check for  
updates

**Citation:** Duan, Y.; Bo, J.; Peng, D.; Li, Q.; Wan, W.; Qi, W. Analysis of Peak Ground Acceleration and Seismogenic Fault Characteristics of the Mw7.8 Earthquake in Turkey. *Appl. Sci.* **2023**, *13*, 10896. <https://doi.org/10.3390/app131910896>

Academic Editors: Bogdan Grecu and Dragos Tataru

Received: 27 August 2023

Revised: 25 September 2023

Accepted: 27 September 2023

Published: 30 September 2023



**Copyright:** © 2023 by the authors. Licensee MDPI, Basel, Switzerland. This article is an open access article distributed under the terms and conditions of the Creative Commons Attribution (CC BY) license (<https://creativecommons.org/licenses/by/4.0/>).

## 1. Introduction

The term “strong motion” refers to the intense shaking experienced during an earthquake. It is a measure of ground acceleration, velocity, and displacement. Observing entails the documentation of acceleration time–history curves of ground motion occurring during earthquakes, with the purpose of studying the characteristics of ground motion and the

response of engineering structures. The exploration of this subject matter has emerged as a pivotal field of study within contemporary seismology and earthquake engineering.

The Anatolian Peninsula is recognized as a highly dynamic seismotectonic area, characterized by a significant occurrence of destructive earthquakes throughout the last century. To monitor such events, Turkey has deployed a substantial number of strong motion accelerographs since 1973 [1]. At the beginning, the network initiated its activity with 67 analog accelerometers. Starting in 1993, digital accelerometers were gradually integrated into the network. From 2000 to 2012, the network expanded to 500 stations that used real-time data transmission systems. The data from these stations were also used for disaster management purposes, such as early warning and emergency response [2]. At present, there are a total of 762 operational strong motion stations that are actively producing approximately 20,000 strong motion records on an annual basis [2,3]. These records provide crucial data for earthquake disaster defense and emergency response.

Scholars from various countries have conducted extensive research based on Turkey's seismic network and strong motion records. In their study, Akkar et al. [4] conducted an analysis of earthquake spectral characteristics, attenuation laws, and near-field effects. Their research aimed to gain a deeper understanding of the physical mechanisms behind ground motion and to enhance seismic hazard assessment. Beyhan et al. [5] examined the correlation between strong motion records and various categories of structural seismic performance, damage patterns, and vulnerability curves. Their research aimed to gather data and insights that could be used to evaluate structural seismic damage and develop seismic design guidelines. Bommer et al. [6] established a shallow crustal ground motion prediction model, offering a reliable tool and parameters for nonlinear dynamic analysis. In addition to these studies, there are also other aspects that have been explored or can be explored using Turkey's strong motion data, such as site effects [7], source characteristics [8], seismic wave propagation [9], seismic intensity [10], seismic risk mapping [11], seismic early warning [12], seismic resilience [13], etc. These aspects are important for advancing the scientific knowledge and practical applications of strong motion data in Turkey and beyond. Nevertheless, in terms of research direction, there is still a lack of studies that combine strong motion records with the relationship to seismogenic faults. Moreover, a comprehensive analysis of the influence of various fault types, locations, and geometric configurations on strong ground motion might be currently lacking.

The objective of this study was to gather and systematically arrange strong motion records obtained from the Mw7.8 earthquake that took place in Turkey on 6 February 2023. The spatial distribution patterns and characteristics of strong ground motion in this earthquake were analyzed. This report provides a summary of the correlation between ground motion and the resulting seismic damage. Additionally, it explores the association between strong motion records and seismogenic faults. Preliminary analyses were conducted concerning near-fault effects, locked segment effects, and trampoline effects based on the geometric features of seismogenic faults. The research presented offers essential insights into the seismogenic mechanism, damage patterns, and characteristics of the earthquake under investigation. Additionally, it functions as a fundamental framework for conducting comprehensive investigations on seismic characteristics and strong motion patterns in Turkey.

## 2. Regional Tectonics and Earthquake Overview

Turkey is located at the convergence of Eurasia, on the Anatolian Plate, which is affected by the interaction of several adjacent plates and fault zones [14], as shown in Figure 1: The Arabian Plate squeezes the Anatolian Plate to the northwest, forming the East Anatolian Fault Zone that is the most active fault zone in Turkey in recent years; The African Plate, located south of Turkey, subducts northward under the Eurasian Plate, forming the Greek Island Arc, which is the most active subduction zone in Europe; The Eurasian Plate, located north of Turkey, compresses Turkey's northern part southward, forming the North Anatolian Fault Zone, which is a right-lateral strike-slip fault zone

extending from the northwest of Turkey to the east of Georgia, and also the longest fault zone in Turkey [15–17].

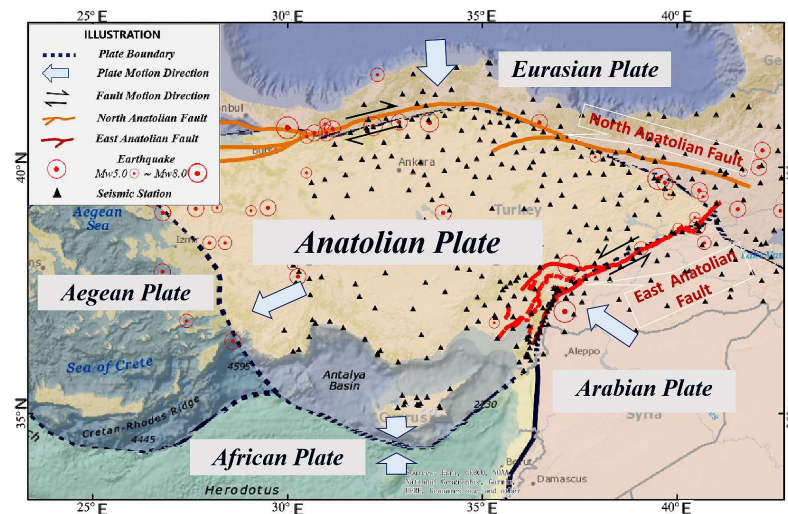


**Figure 1.** Schematic diagram of the relevant plates and active faults around Turkey. (The plate boundaries are depicted by blue dashed lines. The motion directions of the plates are indicated by light blue thick arrows. The East Anatolian Fault (EAF) and the North Anatolian Fault (NAF) are shown by red and orange curves, respectively. The motion of the faults is indicated by dark blue bidirectional arrows. The seismic stations are depicted by black triangles. The figure also shows the earthquakes with Mw 5.0 or above that occurred within and around the Anatolian Plate since 1900. The epicenters are depicted by circles with solid dots, and the size of the circles corresponds to the earthquake magnitude. This figure demonstrates the complex tectonic setting of Turkey and the high seismic hazard in the region).

The exact time of this earthquake was 01:17 (UTC) on 6 February 2023, and its seismogenic fault was a segment of the East Anatolian Fault Zone [18]. The fault zone stretches about 700 km from the eastern to the central-southern part of Turkey, forming a deformation-type tectonic boundary between the Anatolian Plate and the northward-moving Arabian Plate. The slip rate in the eastern part is 6–10 mm/year, and in the western part is 1–4 mm/year [19]. The fault can also be divided into different directions of secondary faults, with mostly left-lateral slip, and locally showing thrust or normal faults [18].

The epicenter was located in Pazarcık district of Kahramanmaraş city in Gaziantep province of Turkey, with a focal depth of 10 km. This earthquake caused extremely severe disasters in southern Turkey and northern Syria and was the strongest earthquake in the region in more than a hundred years [20]. (See Table 1 for details of the earthquake).

The earthquake caused a direct economic loss of USD 34.2 billion [21] in Turkey and resulted in massive casualties and building damage. It killed 59,259 people, which made it the deadliest one in Turkey since 1900 [21]. Gaziantep city was the most severely affected city, with more than 15,000 people dead and more than 30,000 injured. The Şehitkamil district, which was closest to the epicenter, had 12,141 buildings destroyed or severely damaged, with a building damage rate of more than 80% [20]. The Gaziantep Castle was the oldest building damaged in the earthquake, with a history of more than two thousand years, and it possessed extremely precious cultural value [22]. Figure 2 shows the comparison of the castle before and after the earthquake. The earthquake also caused serious disasters in Hatay, Kahramanmaraş, Malatya, Adıyaman, Diyarbakır, Şanlıurfa, Mardin, and other cities and regions. These seismic damages included building collapse (see Figure 3), surface rupture (see Figure 4), landslide (see Figure 5), sand soil liquefaction (see Figure 6), and so on [23–25].

**Table 1.** Statistical table of the earthquake's basic information [20,21].

Basic Facts	Date and Time	6 February 2023, 01:17 (UTC)
	Location	Pazarcık
	Latitude (°)	37.288
	Longitude (°)	37.043
	Earthquake magnitude	Mw7.8
Seismogenic Structure	Hypocentral depth (km)	10
	Fault	East Anatolian Fault
	Rupture Length (km)	70
Peak Value	PGA (cm/s <sup>2</sup> )	2039.20
	PGV (cm/s)	186.78
	PGD (cm)	142.08
Damage Loss	Direct physical damages (USD)	34.2 Billion
	Casualty	59,259

**Figure 2.** Comparison of Gaziantep Castle before (**left**) and after (**right**) the earthquake, showing the damage to the walls and towers. The images were obtained from Google Earth Pro, with the lat long coordinates of 37°04' N, 37°23' E.**Figure 3.** Comparison of Trend Garden Residence Hotel before (**left**) and after (**right**) the earthquake, showing the collapse of the building. The images were obtained from Google Earth Pro, with the lat long coordinates of 38°20' N, 38°17' E.**Figure 4.** Comparison of surface rupture before (**left**) and after (**right**) the earthquake, showing the displacement and cracking of the soil along a fault line. The images were obtained from Google Earth Pro, with the lat long coordinates of 38°20' N, 38°17' E and the date of 5 August 2022 (before) and 15 February 2023.



**Figure 5.** Comparison of a landslide before (**left**) and after (**right**) the earthquake, showing the movement and deposition of soil and rocks on a slope. The images were obtained from Google Earth Pro, with the lat long coordinates of 37°00' N, 36°35' E and the date of 27 December 2022 (before) and 7 February 2023.



**Figure 6.** Comparison of site liquefaction before (**left**) and after (**right**) the earthquake, showing the formation and expulsion of water and sand on a flat area. The images were obtained from Google Earth Pro, with the lat long coordinates of 36°15' N, 36°14' E and the date of 22 December 2022 (before) and 14 February 2023.

### 3. Materials and Methods

#### 3.1. Data Sources

The strong motion data utilized in this study were acquired from Turkey's Disaster and Emergency Management Authority (AFAD). The AFAD operates the National Strong Motion Network that consists of 762 stations distributed all over Turkey. The network records the ground acceleration during earthquakes with magnitudes greater than 3.0. The data are stored and transmitted in a MiniSEED format, which contains the waveform samples, the station metadata, and the timing information. Following the occurrence of the earthquake, the aforementioned agency promptly disseminated pertinent strong motion record data on its official website. Subsequently, the data underwent several calibrations and updates [26]. The data used in this study are from the version published on 1 June 2023, comprising records from 379 stations. The distribution of peak ground acceleration (PGA) and station locations is shown in Figure 7. The strong motion instruments and sensor models for each station are listed below. There are a total of 87 stations that are equipped with the GEOSIG GMS AC-73 seismic instrument. Additionally, there are 140 stations that utilize the Guralp CMG-5T instrument. Furthermore, there are 107 stations that make use of the SARA ACEBOX sa10 instrument. Lastly, there are 45 stations that employ various other seismic instruments [27]. Table 2 presents a compilation of strong motion records acquired from the earthquake under consideration. The table includes relevant details such as station numbers, latitude and longitude coordinates, peak ground acceleration (PGA) values, epicentral distances, fault distances, and station locations. This information has been included in the table due to spatial constraints.

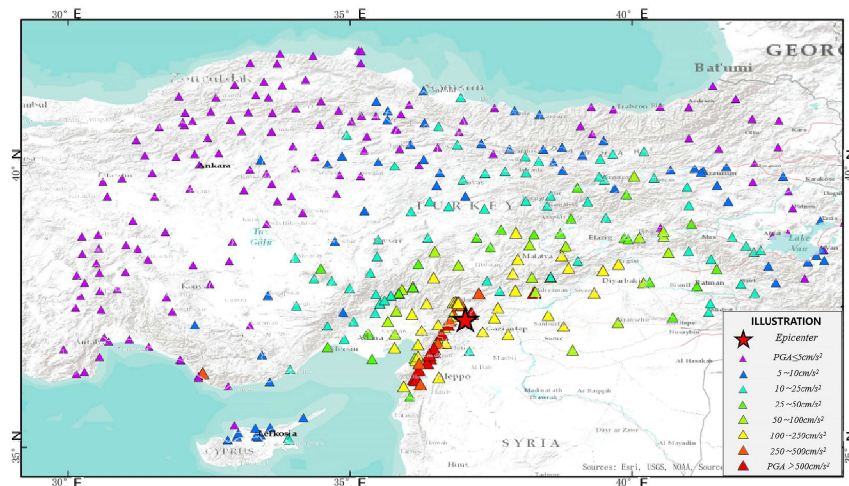


Figure 7. Distribution of seismic recording stations and PGA.

Table 2. Compilation table of seismic recording data.

Station	District	Lon.	Lat.	Repi. (km)	Rrup. (km)	PGA_E (km)	PGA_N (km)	PGA_U (km)
0208	Gölbaşı	37.653	37.787	77.255	1.67	14.00	30.20	16.97
0214	Çelikhan	38.226	38.028	132.738	2.91	54.38	61.68	69.91
2712	Nurdağı	36.732	37.184	29.85	1.10	592.35	555.59	313.75
2718	İslahiye	36.627	37.008	48.33	1.45	630.31	654.43	592.28
3123	Hatay	36.160	36.214	142.92	1.72	593.94	655.57	867.58
3125	Hatay	36.133	36.238	142.09	5.15	1121.95	822.62	1151.56
3129	Defne	36.134	36.191	146.39	2.42	1198.74	1351.50	716.94
3134	Dörtyol	36.205	36.828	90.39	28.95	203.91	246.11	141.51
3135	Arsuz	35.883	36.409	142.23	33.44	1372.07	740.97	588.97
3137	Hatay	36.489	36.693	82.46	0.39	670.17	428.37	448.37
4614	Kahramanmaraş	37.298	37.485	31.42	6.81	2039.20	2016.99	1582.62
4615	Kahramanmaraş	37.138	37.387	13.82	11.28	556.65	584.65	656.68
4626	Onikişubat	36.915	37.575	33.84	16.15	223.09	108.81	112.27
4702	Midyat	41.357	37.417	381.59	248.63	21.33	0.38	15.82
7901	Kilis	37.112	36.709	64.57	50.92	16.55	53.11	50.14
8002	Osmaniye	36.562	37.192	44.01	14.19	202.89	242.95	336.56
8004	Kadirli	36.100	37.380	181.86	168.43	181.86	168.42	71.780

### 3.2. Strong Motion Record Screening and Processing

During the initial screening of the raw data, the study observed a phenomenon in which a small number of station records displayed ‘truncated’ characteristics. For instance, at Station 0208 (as shown in Table 2), despite being only 1.67 km away from the fault, the recorded PGA was only around 30 cm/s<sup>2</sup> (significantly lower than the average acceleration within 5 km of the fault, which exceeds 500 cm/s<sup>2</sup>). The record had a duration of fewer than 8 s. Station 0214 demonstrated analogous behavior, as it was located at a distance of 2.91 km from the fault and experienced a peak acceleration below 70 cm/s<sup>2</sup>. Nineteen stations in the acquired strong-motion records displayed the previously mentioned ‘truncated’ characteristics. Further analysis revealed that most of these stations were located closer to the fault or epicenter. Additionally, it should be noted that station 4702 exhibited a deficiency in its seismic motion records. Specifically, this station only captured seismic motion along the east–west and vertical axes, while lacking data for the north–south direction. The recorded magnitudes were approximately 15 cm/s<sup>2</sup> for the east–west and vertical directions, whereas the north–south direction only registered a magnitude of 0.4 cm/s<sup>2</sup>. To ensure data accuracy, this study excluded the aforementioned 20 records that potentially had anomalous data.

The strong motion data are subject to various issues that can affect their accuracy and consistency, such as instrument errors, baseline drift, and digitization distortion. To avoid such problems, we have followed the standard procedures and methods for processing and correcting our data, such as applying filters, removing outliers, interpolating missing values, etc. Moreover, we have verified our data with other sources, such as seismic stations, satellite images, etc., to ensure their validity and usefulness.

We processed the acceleration data in two steps, using two different software programs. First, we used MATLAB Software (Version R2016a) to perform batch processing of the raw data from all stations, which included converting the data format, extracting the time and amplitude values, and synchronizing the time stamps. Second, we used SeismoSignal software (Version 5.1.0) to perform further processing of the selected records that showed significant PGA values or interesting features, such as station 4614. This involved performing a baseline correction to remove any drift or offset in the data and applying Butterworth high-pass filtering to eliminate any low-frequency noise or artifacts in the data.

### 3.3. Preliminary Analysis of the Characteristics of PGA Distribution

According to Table 2, the earthquake's highest Peak Ground Acceleration (PGA) values were recorded at station 4614, which is situated in Kahramanmaraş City. Its PGA values in all three directions were the largest among all stations (north–south:  $2039.20 \text{ cm/s}^2$ , east–west:  $2016.99 \text{ cm/s}^2$ , vertical:  $1582.62 \text{ cm/s}^2$ ). We used SeismoSignal software (Version 5.1.0) to replot the data from station 4614, using a smoothing spline function to reduce noise and enhance clarity. Figure 8 displays the PGA time–history curve pertaining to station 4614. The PGA value of  $1372.07 \text{ cm/s}^2$ , which ranks as the second-largest in the east–west direction, was documented at station 3135 in Arsuz. This measurement was obtained at a fault distance of 33.44 km. The second-largest north–south PGA value ( $1351.50 \text{ cm/s}^2$ ) was recorded at station 3129 in Defne, with a fault distance of 2.42 km. The second-largest vertical PGA value ( $1151.56 \text{ cm/s}^2$ ) was recorded at station 3129 in Hatay, with a fault distance of 5.15 km.

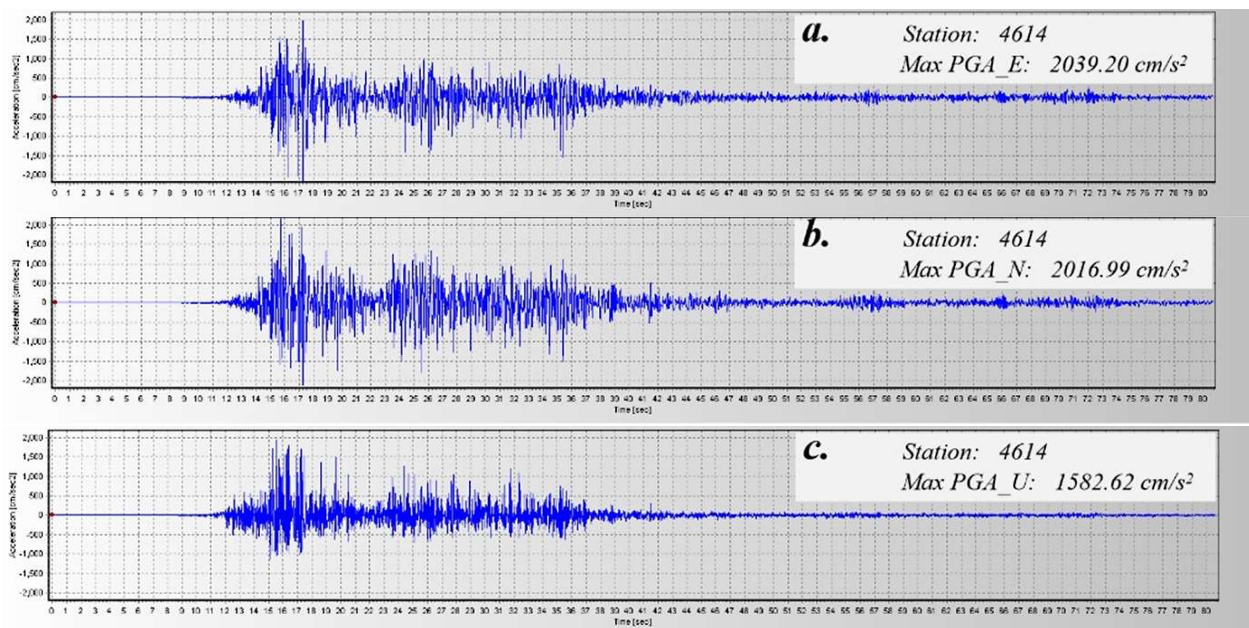


**Figure 8.** PGA time–history curve for station 4614. This figure shows the acceleration time history curves recorded at station 4614 during the earthquake. The subfigures (a–c) represent the east–west, north–south, and vertical components of the acceleration, respectively.

Furthermore, it has been observed that certain north–south peak ground acceleration (PGA) values exhibited a notable disparity when compared to the east–west PGA values in the context of this earthquake. Station 7901, situated in Kilis, exhibited a north–south peak acceleration of  $53.11 \text{ cm/s}^2$ , which is 3.2 times greater than the east–west peak acceleration of  $16.55 \text{ cm/s}^2$ . Similarly, for some stations, the east–west peak acceleration was notably larger than the north–south component. For instance, station 4626 in Onikişubat had an east–west peak acceleration of  $223.09 \text{ cm/s}^2$ , which is 2.05 times that of the north–south peak acceleration ( $108.81 \text{ cm/s}^2$ ). Instances were observed where the vertical peak acceleration surpassed the magnitude of acceleration in the horizontal direction. An example of this can be seen at station 3123 in Hatay, where the vertical peak acceleration measured was  $867.58 \text{ cm/s}^2$ . This value is 1.46 times higher than the east–west peak acceleration recorded at  $593.94 \text{ cm/s}^2$ .

The recorded data comprises information gathered from multiple stations, with a specific focus on strategically positioning some of these stations near the East Anatolian Fault. The nearest station to the fault is station 3139, located at a distance of only 0.06 km. There are additional stations in close proximity to station 3137, such as station 3123 which is located 1.72 km away. There are a total of 22 stations located within a 10 km radius of the fault, while 49 stations are situated within a 50 km radius. The acquisition of near-fault seismic records is of utmost importance in order to gain a comprehensive understanding of near-field seismic characteristics. These records play a vital role in establishing precise attenuation relationships and revealing the scale and faulting characteristics of seismic faults [28,29].

Using Surfer Software (Version 23.0.15), we employed the Kriging interpolation to generate contour maps of the PGA values for three directions (north–south, east–west, and vertical) based on the collected strong motion data. Figure 9 depicts the spatial distribution of Peak Ground Acceleration (PGA) values observed in the earthquake event, which shows a clear correlation with the fault geometry and rupture pattern. In the subsequent sections, we conduct a more detailed analysis and discussion of the seismic effects, building upon the examination of Figure 9.

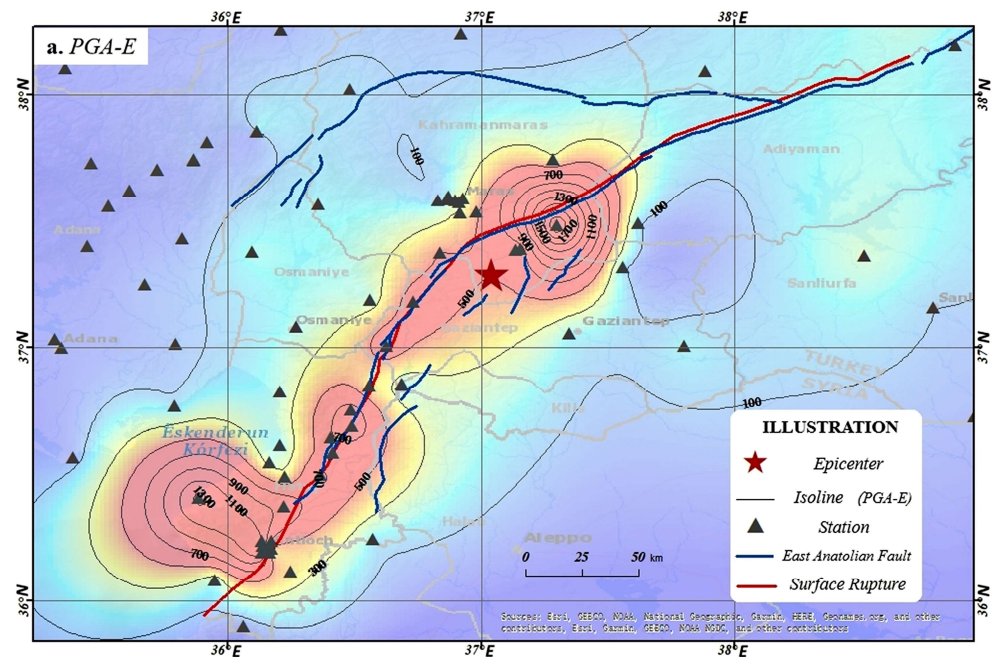
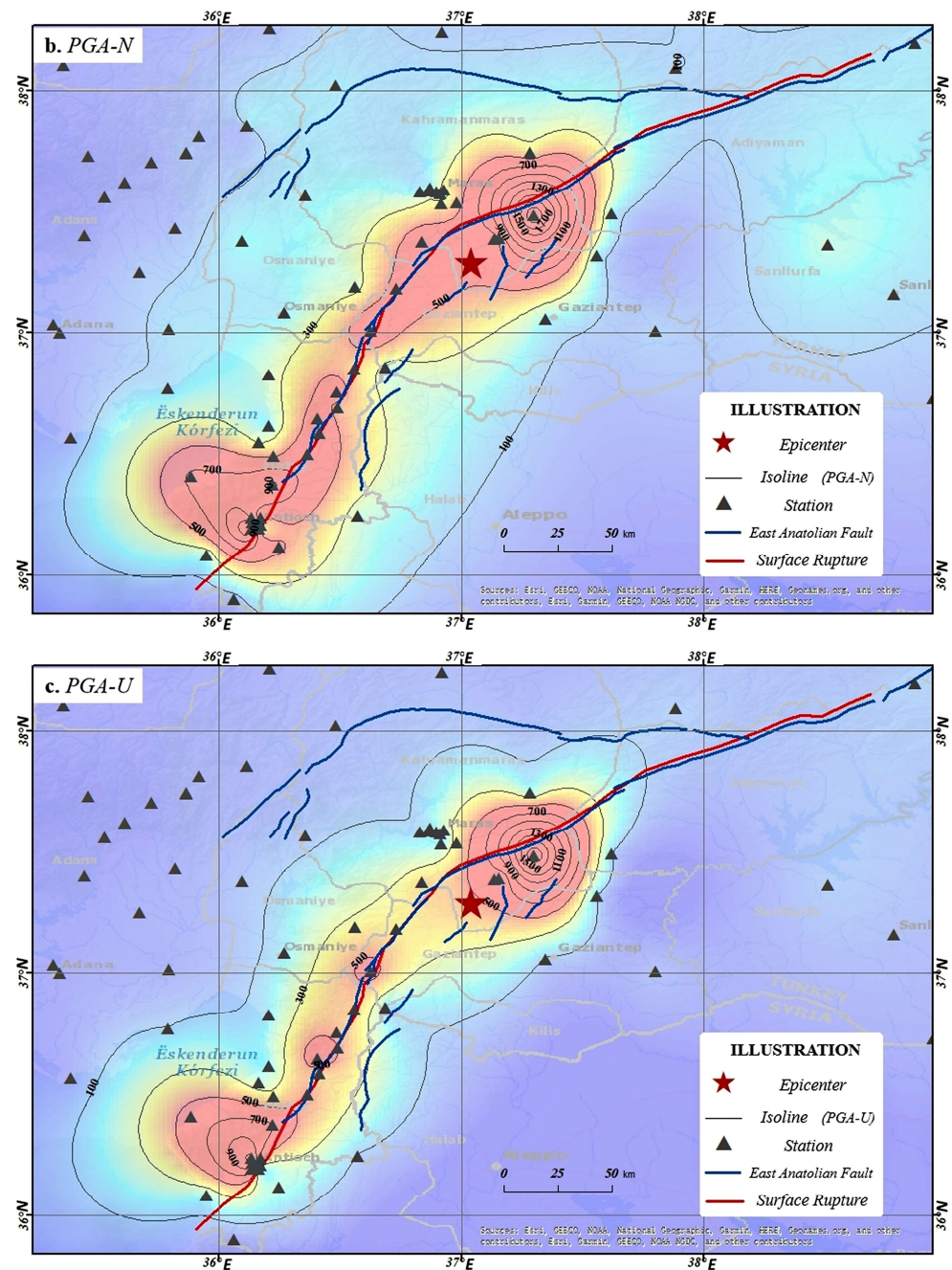


Figure 9. Cont.



**Figure 9.** Isoline Map of PGA for the 2023 Turkey Earthquake (Mw7.8). (This map illustrates the distribution of peak ground acceleration observed in this earthquake with a contour interval of  $100 \text{ mm/s}^2$ . (a–c) are the isopleth maps of peak ground acceleration corresponding to the east–west component, the north–south component, and the vertical component, respectively. The blue lines represent the segments of the East Anatolian fault that ruptured during the earthquake, as well as some adjacent segments that did not rupture but are considered active. The surface rupture is taken from AFAD (2023) “Preliminary Evaluation Report on 6 February 2023 Pazarcik (Kahramanmaraş) Mw 7.7 Elbistan (Kahramanmaraş) Mw 7.6 Earthquakes”).

#### 4. Discussion

##### 4.1. Discussion on Concentration of Near-Fault Strong Ground Motions

The presence of ample seismic damage data suggests that regions located near fault lines tend to experience the most extensive and severe damage [30]. Research conducted on significant earthquakes, such as the Chi-Chi Earthquake, Chilean Earthquake, Wenchuan

Earthquake, Hanshin Earthquake, and New Zealand Earthquake [31,32] have consistently demonstrated that both strong motion observations and numerical simulations indicate a concentration of intense ground motions within a narrow annular region that is centered on the surface projection of the fault [33]. The concentration of strong ground motion is primarily attributed to the geometric attenuation of seismic wave energy radiated from the fault slip source [34]. Analyzing Figure 9, it is evident that the strong ground motions along the fault rupture of this earthquake in Turkey exhibit a clear concentration effect. The distribution of contour lines along the East Anatolian Fault rupture zone exhibits a belt-like pattern, which is consistently observed for peak accelerations in all three directions.

The presence of high levels of ground motion in close proximity to active faults indicates a consistent distribution pattern that reflects the characteristics of the fault zone and its seismic activity. The investigation of the correlation between the distribution region of intense ground motion and parameters such as earthquake magnitude, fault depth, fault type, and the rupture process of the fault is of utmost importance in the field of near-fault ground motion research, because it can reveal the spatial variation and complexity of ground motion along a fault zone. In this study, we focus on the East Anatolian Fault Zone (EAFZ), which is a major left-lateral strike-slip fault system in Turkey that has experienced several large earthquakes in history. The EAFZ consists of several segments with different geometries, slip rates, and rupture lengths. The EAFZ also exhibits various types of surface ruptures, such as distributed cracks, en echelon fractures, pull-apart basins, and slope failures. These features influence the propagation and amplification of seismic waves along the fault zone.

To support our argument that the intensity of near-fault ground motion decreases notably with increasing fault distance, we cite studies by Inoue et al. [33] and Liu et al. [34] who utilized dynamic and kinematic source models to investigate the relationship between strong ground motion distribution and parameters such as fault distance and reported consistent results. The statistical analysis in this study focuses on the three-component peak ground acceleration (PGA) data located within a 30 km radius of the fault. The specific details can be found in Table 3. Based on the findings, it can be concluded that the average peak acceleration within a 10 km radius of the fault surpasses  $500 \text{ cm/s}^2$ . Similarly, within a 20 km radius, the average peak acceleration exceeds  $200 \text{ cm/s}^2$ , while within a 30 km radius, it surpasses  $100 \text{ cm/s}^2$ . The study also investigates the relationship between peak acceleration and fault distance, as depicted in Figure 10. Clear trends show that peak acceleration significantly attenuates with increasing fault distance. These statistical findings support the conclusions from numerical simulation studies.

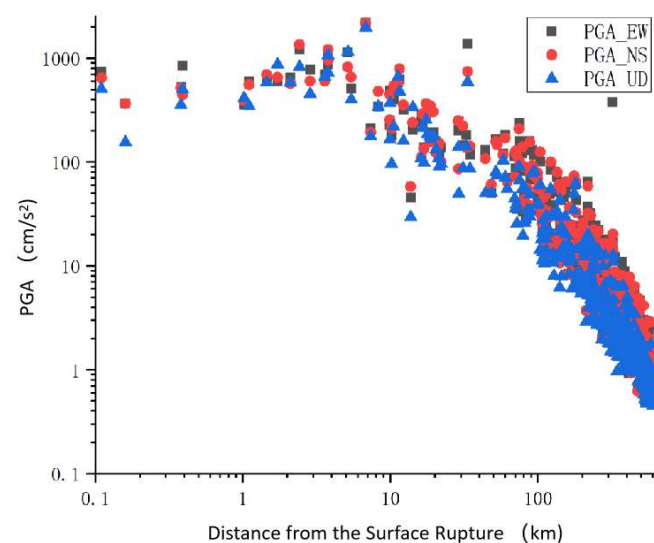


**Figure 10.** Scatter plot of PGA against fault distance.

**Table 3.** Statistics of PGA for near-fault (the radial distance < 30 km) seismic records.

Fault Distance (km)		0--5	5--10	10--15	15--20	20--25	25--30
Mean PGA (cm/s <sup>2</sup> )	Horizontal	692.49	614.25	314.92	244.64	122.81	135.90
	North–South	674.19	614.40	375.94	250.61	138.02	104.94
	Vertical	561.37	539.45	283.61	172.11	102.38	69.21

4.2. Discussion on Locked Segment Effect

Locked segments are defined as the areas of non-uniform contact between two fault planes. Additionally, they encompass sections of the fault that have not yet experienced rupture [35]. Existing research suggests that the movement mode and seismic activity of a fault are influenced by locked segments, and breakthroughs in these locked segments lead to the concentrated release of seismic energy [36]. Prior studies by Qin et al. (2010) [37] and Yang et al. (2017) [38] have validated the locked segment rupture theory through the retrospective analysis of typical large earthquakes.

According to the illustration presented in Figure 11, the East Anatolian Main Fault exhibits a division into nine secondary sub-faults. These sub-faults encompass the Amanos FS Segment and the Pazarcik Segment. Every individual sub-fault demonstrates distinct characteristics, including the occurrence of folding and overlapping. Duman et al. (2013) [39], based on active fault mapping and utilizing seismic data from Turkey, confirmed the discontinuous segmented structure of the East Anatolian Fault Zone. Additionally, the authors provided further details regarding the geometric segmentation, intermittent nature of activity, and regional characteristics associated with induced earthquakes.

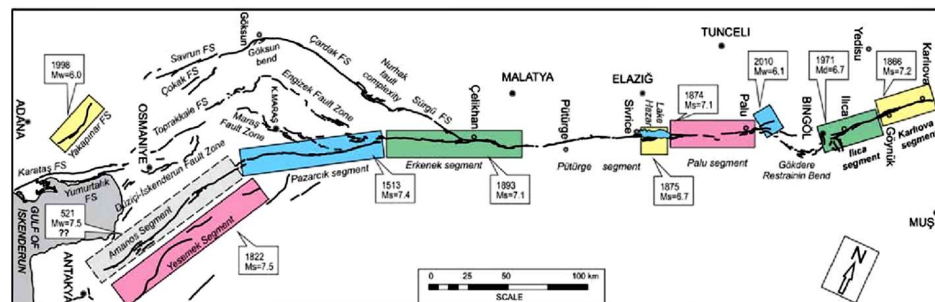


**Figure 11.** Schematic diagram of surface rupture segments and earthquake of the East Anatolian Fault and its sub-segments [39].

According to the illustration presented in Figure 11, the East Anatolian Main Fault exhibits a division into nine secondary sub-faults. These sub-faults encompass the Amanos FS Segment and the Pazarcik Segment. Every individual sub-fault demonstrates distinct characteristics, including the occurrence of folding and overlapping. Duman et al. (2013) [39], based on active fault mapping and utilizing seismic data from Turkey, confirmed the discontinuous segmented structure of the East Anatolian Fault Zone and inferred that each segment has a different slip rate, rupture length, and recurrence interval. Additionally, the authors provided further details regarding the geometric segmentation, intermittent nature of activity, and regional characteristics associated with induced earthquakes and suggested that these factors affect the seismic hazard assessment of the region. These inferences are important for our research work because they help us understand the spatial distribution and variation in ground motion along the East Anatolian Fault Zone and its sub-faults.

Upon further examination of Figure 9, it is evident that the distribution of peak ground motion is not continuous. Instead, it is concentrated within specific fault segments, including the Pazarcik Segment, the Maras Fault Zone, the Amanos FS Segment, and the Islahiye releasing bend. This concentration is observed in addition to the band-like concentration along the fault rupture. Figure 12 delineates four distinct regions characterized by significant ground motion peaks, as outlined below.

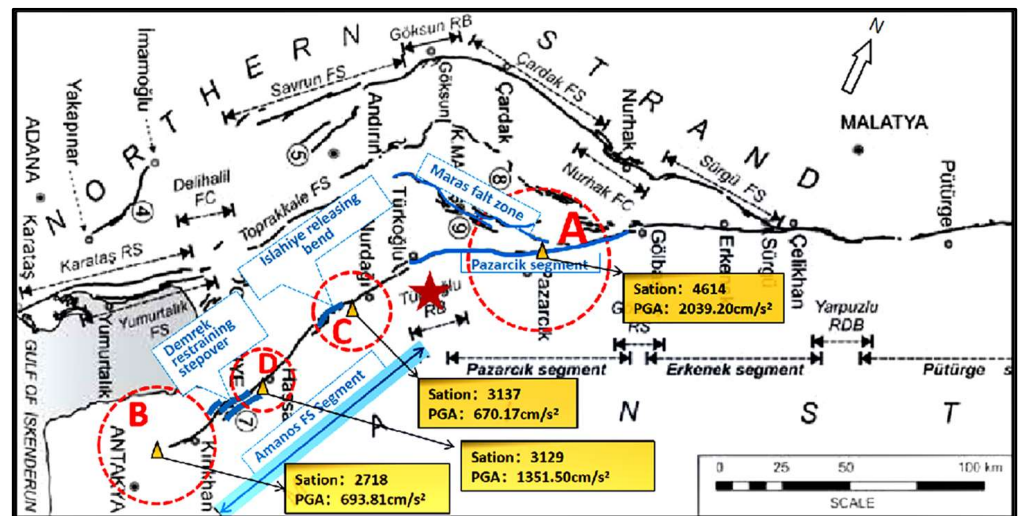


Figure 12. Distribution of high-value PGA near locked fault segments.

Region A is located in close proximity to the boundary between the Pazarçik Segment, which is a primary segment of the East Anatolian Main Fault, and the Maras Fault Zone, which is a secondary sub-fault of the East Anatolian Fault. Centered around station 4614 in Kahramanmaraş city (coordinates  $37.485^{\circ}$  N,  $37.298^{\circ}$  E), the peak acceleration reaches  $2039.20 \text{ cm/s}^2$  at a distance of 31.42 km from the epicenter.

Region B is located at the southwestern end of the Amanos FS Segment, which is a primary segment of the East Anatolian Main Fault. This region serves as the southernmost boundary of the Anatolian Fault. Centered around station 2718 in İslahiye city (coordinates  $37.008^{\circ}$  N,  $36.627^{\circ}$  E), the peak acceleration is  $693.81 \text{ cm/s}^2$  at a distance of 48.30 km from the epicenter.

Region C is situated in close proximity to the bending point of the Amanos FS Segment, more specifically known as the Islahiye releasing bend. Centered around station 3137 in Hatay city (coordinates  $36.489^{\circ}$  N,  $36.693^{\circ}$  E), the peak acceleration is  $670.17 \text{ cm/s}^2$  at a distance of 82.46 km from the epicenter.

Region D is near the left-lateral faulting area of the Amanos FS Segment, known as the Demrek restraining stepover. Centered around station 3129 in Defne city (coordinates  $36.191^{\circ}$  N,  $36.134^{\circ}$  E), the peak acceleration reaches  $1351.50 \text{ cm/s}^2$  at a distance of 146.39 km from the epicenter.

The four regions are situated in close proximity to local overlaps, bends, or terminations of the East Anatolian Fault. These areas frequently exhibit concentrated stress patterns and experience multiple reflections and refractions of seismic waves, which are further influenced by inertia forces. This combination of factors makes these regions prone to experience elevated ground motion [37,40,41]. The concentrated distribution of peak ground motion in these four regions signifies the locked segment effects and suggests higher ground motion intensity and severe seismic damage near these segments.

#### 4.3. Discussion on the Trampoline Effect

In seismic design, the influence of vertical ground motion on structural responses may need to be considered, and this influence is often specified by a certain ratio of horizontal ground motion [40]. Generally, the vertical acceleration is about 1/2 to 2/3 of the horizontal one [41]. With the development of strong motion technology, the number of strong motion stations has increased rapidly, and more near-field strong motion records have been obtained, giving people a deeper and more comprehensive understanding of strong motion records. Especially in recent years, more and more earthquake records with larger vertical peak accelerations have drawn people's attention.

The trampoline effect refers to the phenomenon that when seismic waves reach the ground surface, the surface layer will be compressed and bounced up, just like a trampoline. When the surface layer recovers its elasticity, it will produce an upward reaction force, which will increase the ground acceleration (as shown in Figure 13). The trampoline effect was first observed in the 2008 Mw6.9 Iwate-Miyagi earthquake in Japan [42], and later reported in other earthquakes, such as the 2010 Mw7.2 El Mayor-Cucapah earthquake in Mexico [43], and the 2016 Mw7.8 Kaikoura earthquake in New Zealand [44]. In these earthquakes, it was observed that the vertical acceleration was significantly larger than (or even several times larger than) the horizontal acceleration, and the vertical upward acceleration was significantly larger than the downward acceleration. Aoi S. et al. studied the  $3866 \text{ cm/s}^2$  vertical acceleration produced by the Mw6.9 Iwate-Miyagi earthquake on 14 June 2008 and found that the vertical ground acceleration showed a clear asymmetry, with the peak value in the upward direction being about 1.6 times that in the downward direction.

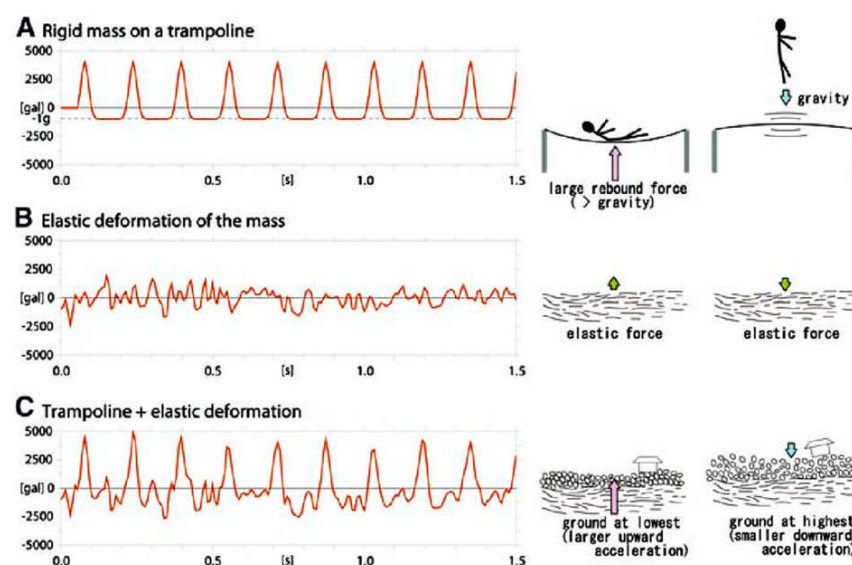
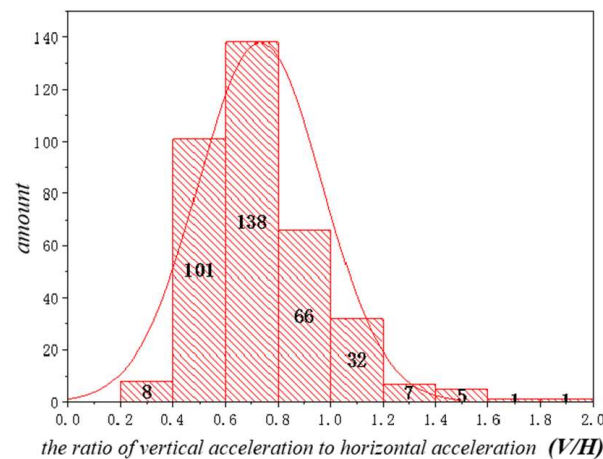


Figure 13. Schematic diagram of the trampoline effect [42].

The main factors that affect the trampoline effect are the seismic wave characteristics, the ground properties, and the topography. The seismic wave characteristics include the frequency content, amplitude, duration, and incidence angle of the seismic waves. Some site conditions may enhance or reduce the trampoline effect. For example, soft soils with low stiffness and high damping may amplify seismic waves more than hard rocks with high stiffness and low damping. Layered grounds with impedance contrasts may reflect or refract seismic waves more than homogeneous grounds.

This paper calculates the ratio of vertical ground motion to horizontal ground motion peak acceleration ( $V/H$ ) and its relationship with the number of stations, as shown in Figure 14. The analysis shows that there were 172 stations with a vertical-to-horizontal acceleration ratio greater than  $2/3$  in this earthquake motion, accounting for 48% of the total number of records. By further analyzing typical vertical and horizontal acceleration records, the paper finds that station 3123 located in Hatay city (coordinates  $36.160^\circ \text{ E}$ ,  $36.214^\circ \text{ N}$ , fault distance 1.72 km) has a vertical peak acceleration of  $867.58 \text{ cm/s}^2$ , which was 1.46 times that of the north–south direction ( $593.94 \text{ cm/s}^2$ ); more importantly, its vertical upward peak acceleration of  $867.58 \text{ cm/s}^2$  was much larger than its downward peak acceleration of  $470.46 \text{ cm/s}^2$  (the upward direction was 1.84 times that of the downward direction), as shown in Figure 15, is a typical manifestation of the trampoline effect in this earthquake.



**Figure 14.** Distribution curve of acceleration V/H number.

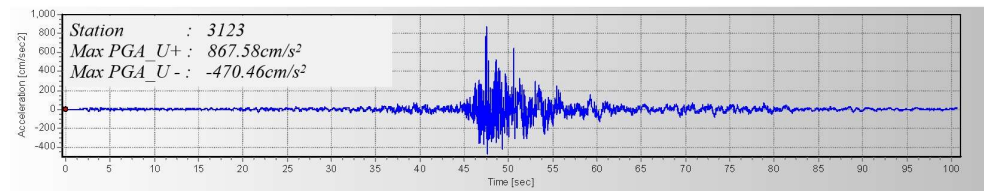


**Figure 15.** Typical vertical acceleration time history curve showing the trampoline effect.

## 5. Conclusions

Turkey is a seismic hotspot due to its location at the boundary between the Eurasian and Arabian tectonic plates, and is characterized by complex interactions between various tectonic plates and fault systems. The Mw7.8 earthquake that occurred on 6 February 2023 was the most devastating earthquake in Turkey since 1900. This study examines the aspects of severe ground motion and their relevance to the fault rupture from a number of different angles, based on information from the Turkish Disaster and Emergency Management Authority (AFAD) and the geometric features of the rupture fault. The primary findings derived from this study can be summarized as follows:

The earthquake resulted in a substantial amount of strong motion record data, with a total of 379 stations capturing the earthquake's effects. Station 4614 recorded the highest peak acceleration ever recorded in Turkey, measuring  $2039.20 \text{ cm/s}^2$  in the north–south direction. The acquisition of near-fault seismic records is of great importance in enhancing our understanding of near-field ground motion and providing insights into the size and slip characteristics of seismic faults.

The phenomenon of the concentration effect of strong ground motion near active faults is readily observable. The distribution of peak accelerations along the near-fault area shows a band-like pattern, with a noticeable trend of decreasing acceleration as the fault distance increases.

The distribution of high-value ground motion was influenced by locked segment effects. The concentration of strong ground motion is observed in four distinct regions along the East Anatolian Fault Zone, which correspond to some special features of the fault geometry and slip distribution.

This earthquake also manifested the trampoline effect. The vertical-to-horizontal acceleration ratio of 172 stations was greater than  $2/3$ , accounting for 48% of the total number of records. Station 3123, located in Hatay city, had a vertical upward peak acceleration of  $867.58 \text{ cm/s}^2$ , which was much larger than its downward peak acceleration of  $470.46 \text{ cm/s}^2$ .

This study provides significant contributions regarding the seismic characteristics, strong motion patterns, and subsequent detailed investigations related to the destruction pattern, characteristics, and seismogenic mechanisms of this particular earthquake.

This paper ignores the influence of permanent ground displacement (residual displacement) in the strong motion data processing, which may exist in some near-source stations due to instrument displacement, tilt, or site liquefaction and other seismic damage phenomena. Because of the lack of reliable data on permanent displacement, this paper excludes these residual displacements, which require further and detailed discussion in future research.

**Author Contributions:** Software, D.P.; validation, W.Q.; data curation, Q.L.; writing—original draft preparation, Y.D. and W.W.; writing—review and editing, Y.D. and D.P.; supervision, J.B. All authors have read and agreed to the published version of the manuscript.

**Funding:** This research was funded by the National Natural Science Foundation of China [grant number U1939209] and the Fundamental Research Funds for the Central Universities [grant number ZY20215121].

**Institutional Review Board Statement:** Not applicable.

**Informed Consent Statement:** Not applicable.

**Data Availability Statement:** The raw data presented in this study are openly available at <https://tadas.afad.gov.tr/map>, accessed on 6 June 2023. The other data used to support the findings of the study are available from the author upon request. The author's email address is duanyushi2023@163.com.

**Acknowledgments:** We gratefully acknowledge the Disaster and Emergency Management Authority (AFAD) of Turkey for providing the strong ground motion records of the stations through their official website. We also thank the editor of Applied Sciences and the anonymous reviewers for their constructive comments and suggestions that improved the quality of our paper.

**Conflicts of Interest:** The authors declare no conflict of interest.

## References

1. Sandıkkaya, M.A.; Yılmaz, M.T.; Bakır, B.S.; Yılmaz, Ö. Site classification of Turkish national strong-motion stations. *J. Seismol.* **2010**, *14*, 543–563. [[CrossRef](#)]
2. Akkar, S.; Çağnan, Z.; Yenier, E.; Erdoğan, Ö.; Sandıkkaya, M.A.; Gülkan, P. The recently compiled Turkish strong motion database: Preliminary investigation for seismological parameters. *J. Seismol.* **2012**, *14*, 457–479. [[CrossRef](#)]
3. Frontiers. Relationship Between Asperities and Velocity Pulse Generation Mechanism. Available online: <https://www.frontiersin.org/articles/10.3389/feart.2022.843532/full> (accessed on 1 June 2023).
4. Akkar, S.; Bommer, J.J. Prediction of elastic displacement response spectra in Europe and the Middle East. *Earthq. Eng. Struct. Dyn.* **2007**, *36*, 1275–1301. [[CrossRef](#)]
5. Beyhan, G.; Keskinsezer, A.; Kafadar, Ö. Analysis of strong ground motion data from the Van earthquake (Turkey), 2011. *Geomech. Geophys. Geo-Energy Geo-Resour.* **2019**, *5*, 253–270. [[CrossRef](#)]
6. Akkar, S.; Bommer, J.J. Empirical equations for the prediction of PGA, PGV, and spectral accelerations in Europe, the Mediterranean region, and the Middle East. *Seismol. Res. Lett.* **2010**, *81*, 195–206. [[CrossRef](#)]
7. Sandeep, S.D.; Parveen Kumar, M.; Kumar, R. Strong motion modelling of the 1999 Izmit Earthquake using site effect in a semi-empirical technique: A more realistic approach. *Pure Appl. Geophys.* **2022**, *179*, 483–497. [[CrossRef](#)]
8. Chen, W.; Rao, G.; Kang, D.; Wan, Z.; Wang, D. Early report of the source characteristics, ground motions, and casualty estimates of the 2023 M<sub>w</sub> 7.8 and 7.5 Turkey earthquakes. *J. Earth Sci.* **2023**, *34*, 297–303. [[CrossRef](#)]
9. Aochi, H.; Durand, V.; Douglas, J. Influence of super-shear earthquake rupture models on simulated near-source ground motion from the 1999 Izmit, Turkey, earthquake. *Bull. Seismol. Soc. Am.* **2011**, *101*, 726–741. [[CrossRef](#)]
10. Askan, A.; Karimzadeh, S.; Bilal, M. Seismic Intensity Maps for the Eastern Part of the North Anatolian Fault Zone (Turkey) Based on Recorded and Simulated Ground-Motion Data. In *Active Global Seismology: Neotectonics and Earthquake Potential of the Eastern Mediterranean Region*; American Geophysical Union: Washington, DC, USA, 2017; pp. 273–287. [[CrossRef](#)]
11. Büyüksaraç, A.; Işık, E.; Bektaş, Ö. A comparative evaluation of earthquake code change on seismic parameter and structural analysis; a case of Turkey. *Arab. J. Sci. Eng.* **2022**, *47*, 12301–12321. [[CrossRef](#)]
12. Cremen, G.; Galasso, C.; Zuccolo, E. Investigating the potential effectiveness of earthquake early warning across Europe. *Nat. Commun.* **2022**, *13*, 639. [[CrossRef](#)]
13. Byun, J.E.; D'Ayala, D. Urban seismic resilience mapping: A transportation network in Istanbul, Turkey. *Sci. Rep.* **2022**, *12*, 8188. [[CrossRef](#)] [[PubMed](#)]
14. Jackson, J.; McKenzie, D. The relationship between plate motions and seismic moment tensors, and the rates of active deformation in the Mediterranean and Middle East. *Geophys. J. Int.* **1988**, *93*, 45–73. [[CrossRef](#)]

15. Jackson, J. Partitioning of strike-slip and convergent motion between Eurasia and Arabia in eastern Turkey and the Caucasus. *J. Geophys. Res. Atmos.* **1992**, *97*, 12471–12479. [CrossRef]
16. Westaway, R.O.B.; Arger, J.A.N. The Gölbaşı basin, southeastern Turkey: A complex discontinuity in a major strike-slip fault zone. *J. Geol. Soc.* **1996**, *153*, 729–744. [CrossRef]
17. Stein, R.S.; Barka, A.A.; Dieterich, J.H. Progressive failure on the North Anatolian fault since 1939 by earthquake stress triggering. *Geophys. J. Int.* **1997**, *128*, 594–604. [CrossRef]
18. Taymaz, T.; Eyidog an, H.; Jackson, J. Source parameters of large earthquakes in the East Anatolian Fault Zone (Turkey). *Geophys. J. Int.* **1991**, *106*, 537–550. [CrossRef]
19. Wang, Z.; Zhang, W.; Taymaz, T.; He, Z.; Xu, T.; Zhang, Z. Dynamic rupture process of the 2023 Mw 7.8 Kahramanmaraş earthquake (SE T urkiye): Variable rupture speed and implications for seismic hazard. *Geophys. Res. Lett.* **2023**, *50*, e2023GL104787. [CrossRef]
20. Ozkula, G.; Dowell, R.K.; Baser, T.; Lin, J.L.; Numanoglu, O.A.; Ilhan, O.; Olgun, C.G.; Huang, C.W.; Uludag, T.D. Field reconnaissance and observations from the February 6, 2023, Turkey earthquake sequence. *Nat. Hazards* **2023**, *119*, 663–700. [CrossRef]
21. World Bank Disaster Assessment Report. Earthquake Damage in T urkiye Estimated to Exceed \$34 billion. Available online: <https://www.worldbank.org/en/news/press-release/2023/02/27/earthquake-damage-in-turkiye-estimated-to-exceed-34-billion-world-bank-disaster-assessment-report> (accessed on 1 June 2023).
22. Karataş, L.; Ateş, T.; Alptekin, A.; Dal, M.; Yakar, M. A systematic method for post-earthquake damage assessment: Case study of the Antep Castle, T urkiye. *Adv. Eng. Sci.* **2023**, *3*, 62–71.
23. Mavroulis, S.; Mavrouli, M.; Vassilakis, E.; Argyropoulos, I.; Carydis, P.; Lekkas, E. Debris Management in Turkey Provinces Affected by the 6 February 2023 Earthquakes: Challenges during Recovery and Potential Health and Environmental Risks. *Appl. Sci.* **2023**, *13*, 8823. [CrossRef]
24. Zenodo. Preliminary Mapping of Liquefaction Phenomena Triggered by the February 6 2023 M7.7 earthquake, T urkiye/Syria, Based on Remote Sensing Data. Technical Report. February 2023. Available online: <https://doi.org/10.5281/zenodo.7668401> (accessed on 1 June 2023).
25. Dal Zilio, L.; Ampuero, J.P. Earthquake doublet in Turkey and Syria. *Commun. Earth Environ.* **2023**, *4*, 71. [CrossRef]
26. Baltzopoulos, G.; Baraschino, R.; Chioccarelli, E.; Cito, P.; Iervolino, I. Preliminary Engineering Report on Ground Motion Data of the Feb. 2023 Turkey Seismic Sequence. *Earthquake reports*, 24 February 2023.
27. Disaster and Emergency Management Authority. Turkish National Strong Motion Network. Department of Earthquake, Disaster and Emergency Management Authority. 1973. Available online: <https://doi.org/10.7914/SN/TK> (accessed on 1 June 2023).
28. Moshou, A.; Konstantaras, A.; Argyrakis, P.; Petrakis, N.S.; Kapetanakis, T.N.; Vardiambasis, I.O. Data Management and Processing in Seismology: An Application of Big Data Analysis for the Doublet Earthquake of 3 March 2021, Elassona, Central Greece. *Appl. Sci.* **2022**, *12*, 7446. [CrossRef]
29. Li, X. Thoughts on the seismic damage phenomena and engineering seismic problems of recent large earthquakes. *Int. Seism. Dyn.* **2001**, *3*, 26–32.
30. Nuti, C.; Briseghella, B.; Lavorato, D.; Taciroglu, E.; Bergami, A.V. Effects of Near-Fault Ground Motions on Civil Infrastructure. *Appl. Sci.* **2023**, *13*, 5929. [CrossRef]
31. Chen, K.H.; Furumura, T.; Rubinstein, J.; Rau, R.-J. Observations of changes in waveform character induced by the 1999 Mw7.6 Chi-Chi earthquake. *Geophys. Res. Lett.* **2011**, *38*, 1–5. [CrossRef]
32. Ulusay, R.; Tuncay, E.; Sonmez, H.; Gokceoglu, C. An attenuation relationship based on Turkish strong motion data and iso-acceleration map of Turkey. *Eng. Geol.* **2004**, *74*, 265–291. [CrossRef]
33. Inoue, T.; Miyatake, T. 3D simulation of near-field strong ground motion based on dynamic modeling. *Bull. Seismol. Soc. Am.* **1998**, *88*, 1445–1456. [CrossRef]
34. Liu, Q.; Yuan, Y.; Jin, X.; Ding, H. Basic characteristics of near-fault ground motion. *Earthq. Eng. Eng. Vib.* **2006**, *2*, 1. [CrossRef]
35. Xu, Q.; Li, W. Study on the distribution of large-scale landslides induced by the Wenchuan earthquake. *J. Eng. Geol.* **2010**, *18*, 818–826.
36. Huang, R. Large-scale landslides and their occurrence mechanisms in China since the 20th century. *Chin. J. Rock Mech. Eng.* **2007**, *182*, 433–454.
37. Qin, S.; Xue, L.; Wang, Y. Further verification of the brittle fracture theory of multi-locked segments of seismogenic faults and discussion on related scientific issues. *Prog. Geophys.* **2010**, *25*, 749–758.
38. Yang, B.; Qin, S.; Xue, L.; Wu, X.W.; Zhang, K. On the equivalence between the cumulative Benioff strain and the shear strain for the locked patches along a seismogenic fault system. *Prog. Geophys.* **2017**, *32*, 1067–1070.
39. Duman, T.Y.; Emre, O. The East Anatolian Fault: Geometry, Segmentation and Jog Characteristics. *Geol. Soc. Lond. Spec. Publ.* **2013**, *372*, 495–529. [CrossRef]
40. Hu, Y. *Seismic Engineering*; Seismological Press: Beijing, China, 1988.
41. Zhou, Z.; Zhou, Y.; Zhao, G. Statistical analysis of peak acceleration ratio and response spectrum in strong earthquake near-field. *Earthq. Eng. Eng. Vib.* **2002**, *22*, 15–18.
42. Aoi, S.; Kunugi, T.; Fujiwara, H. Trampoline effect in extreme ground motion. *Science* **2008**, *322*, 727–730. [CrossRef] [PubMed]

43. Anderson, J.G. Source and site characteristics of earthquakes that have caused exceptional ground accelerations and velocities. *Bull. Seism. Soc. Am.* **2010**, *100*, 1–36. [[CrossRef](#)]
44. Meng, L.; Shi, B.; Liu, J. Comparative analysis of near-field strong ground motion characteristics of the 2010 New Zealand Mw7.0 mainshock and the 2011 Mw6.1 aftershock. *Acta Seismol. Sin.* **2013**, *35*, 351–368.

**Disclaimer/Publisher’s Note:** The statements, opinions and data contained in all publications are solely those of the individual author(s) and contributor(s) and not of MDPI and/or the editor(s). MDPI and/or the editor(s) disclaim responsibility for any injury to people or property resulting from any ideas, methods, instructions or products referred to in the content.